Impact of Jahn-Teller active Mn^{3+} on strain effects and phase transitions in $Sr_{0.65}Pr_{0.35}MnO_3$

Teck-Yee Tan, Brendan J. Kennedy,* Qingdi Zhou, and Christopher D. Ling
The School of Chemistry, The University of Sydney, Sydney, NSW 2006, Australia

Wojciech Miiller
The School of Chemistry, The University of Sydney, Sydney, NSW 2006, Australia and Bragg Institute, ANSTO, PMB1 Menai 2234 NSW, Australia

Christopher J. Howard
The School of Physics, The University of Sydney, Sydney, NSW 2006, Australia

Michael A. Carpenter
Department of Earth Sciences, University of Cambridge, Downing Street, Cambridge CB2 3EQ, United Kingdom

Kevin S. Knight
ISIS Facility, Rutherford Appleton Laboratory, Chilton, Didcot, Oxfordshire OX11 0QX, United Kingdom
(Received 6 November 2011; revised manuscript received 10 February 2012; published 19 March 2012)

The mixed-valence manganite $Sr_{0.65}Pr_{0.35}MnO_3$ has been prepared and its crystal and magnetic structure investigated between 7 and 1200 K using high-resolution powder neutron diffraction. The structural and lattice parameter data have been used to determine the octahedral tilting and spontaneous strains associated with the structural, electronic, and magnetic phase transitions. At room temperature, the structure is tetragonal and is characterized by cooperative out-of-phase tilts of the MnO_6 octahedra about the c axis and a large Jahn–Teller-type distortion due to the presence of Mn^{3+}. The sample exhibits a reversible phase transition from the cubic $Pm\bar{3}m$ perovskite to a tetragonal $I4/mcm$ structure at 750 K. The $Pm\bar{3}m \leftrightarrow I4/mcm$ phase transition is continuous, and the tetragonal strain, which is dominated by the Jahn–Teller-type distortion of the MnO_6 octahedra, exhibits an unusual $e_t^{0.5} \propto (T_c - T)$ temperature dependence. At low temperatures, a C-type antiferromagnetic structure develops with a Neel temperature T_N of 250 K. The Mn magnetic moment at 7 K is 2.99(2) μ_B/Mn. The magnetic ordering introduces additional tetragonal strain, and this strain shows the expected quadratic dependence on the magnetic moment at low temperatures. An increase in the octahedral tilt angle at T_N demonstrates an effective coupling between the magnetic ordering process and octahedral tilting.

DOI: 10.1103/PhysRevB.85.104107 PACS number(s): 61.05.fm, 64.60.Ej, 61.50.Ks

I. INTRODUCTION

Mixed-valent Mn perovskites of the type $Ln_{1-x}A_xMnO_3$, where Ln is a lanthanide and A a divalent cation, have been the subject of enormous research effort for over 50 years,[1] with the discovery of colossal magnetoresistance (CMR) in such oxides driving much of the more recent interest.[2] The rich diversity in electrical, magnetic, and structural phenomena displayed by such oxides is testament to the intricate interplay between the orbital, spin, charge, and lattice degrees of freedom in these oxides. This is in contrast to the behavior of traditional ferromagnets, such as Co, Ni, and Fe, used in many devices where the spin system is isolated from the lattice.[3] In addition to their great potential for magnetic storage technology, A-site doped manganite perovskites have been widely studied as cathode materials for use in solid oxide fuel cells (SOFCs).[4–6]

An important feature of the mixed valence Mn^{3+}/Mn^{4+} manganates is the long-range orbital ordering that arises as a consequence of a Jahn–Teller (JT) type distortion of the formally Mn^{3+} cations. It is generally accepted that replacing the trivalent lanthanide cation with a divalent alkaline earth cation introduces a mixed valence Mn^{3+} and Mn^{4+} array[7–9] where the charge can hop from Mn to Mn via the bridging oxygen anions. A consequence of the relatively large difference in the size of the Mn^{3+} and Mn^{4+} cations (ionic radii of 0.645 vs 0.53 Å, respectively, in a six-coordinate geometry[10]), together with the JT distortion, is that such a substitution is likely to introduce strains into the lattice. However, very little is known about the coupling between the various strains present in such complex oxides.

The present contribution focuses on one member of the well-studied $Sr_{1-x}Pr_xMnO_3$ series,[7,11–13] namely $Sr_{0.65}Pr_{0.35}MnO_3$. Cubic $SrMnO_3$ has a G-type antiferromagnetic (AFM) ground state,[12] whereas $PrMnO_3$ is orthorhombic in $Pnma$ and is an A-type AFM.[14] Knizek *et al.*[7] have previously described the structural, magnetic, and transport properties of several members in the series ($x = 0.15$–0.55) using neutron and x-ray diffraction methods. At low Pr levels ($x \leqslant 0.15$), the oxides are isostructural with cubic $SrMnO_3$ in space group $Pm\bar{3}m$. Increasing the Pr content ($0.25 \leqslant x \leqslant 0.52$) produces a tetragonal structure in $I4/mcm$, while the oxides with Pr contents in the range ($0.52 < x \leqslant 0.55$) are orthorhombic in $Imma$. At still higher Pr contents, the orthorhombic $Pnma$ structure is encountered.[15] This sequence of structures reflects differences in the cooperative tilting of the corner-sharing MnO_6 octahedra and can be correlated with changes in the tolerance factor $t = (r_A + r_O)/\sqrt{2}(r_B + r_O)$, where r_A, r_B, and r_O are the ionic radii of the A, B, and

oxygen ions, respectively. The same sequence of transitions has been observed in other systems, including $Sr_{1-x}Ba_xMO_3$ (M = Hf or Zr)[16,17] and in $SrMO_3$ (M = Zr, Tc, or Ru) upon heating.[18–20] A critical difference between these ABO_3 perovskites and $Sr_{0.65}Pr_{0.35}MnO_3$ is the presence of the JT active Mn^{3+} cation in the latter.

In this paper, the evolution of the crystal structure of $Sr_{0.65}Pr_{0.35}MnO_3$ from 7 to 1000 K is described from high-resolution powder neutron diffraction data. Below 750 K, the structure is tetragonal, and we describe the influence of three phenomena, octahedral tilting, JT distortion, and magnetostriction on the structure. We observe the formation of superparamagnetic clusters and long-range magnetic ordering and describe how these impact the local structures.

II. EXPERIMENTAL

The reagents used for the syntheses were obtained from Sigma-Aldrich and AITHACA and were of at least 99.9% purity. Prior to use, $SrCO_3$ and MnO_2 were dried overnight at 120 °C for 48 h, and the praseodymium oxide was heated overnight at 1000 °C. Stoichiometric amounts of $SrCO_3$, Pr_6O_{11}, and MnO_2 were mixed by hand and preheated in a furnace at 850 °C in air for 24 h and then fired at 1200 and 1400 °C for 24 h with intermediate grindings. The powder was then pressed into 10-mm diameter pellets, and these were sintered in air at 1500 °C for 48 h. The sample was cooled down to 800 °C, held at this temperature for 6 h, and then cooled to room temperature at a rate of 15 °C/min. The sample purity was monitored using a Panalytical powder x-ray diffractometer employing Cu K alpha radiation.

Neutron diffraction data were collected on an approximately 20 g sample at the 1-m position of the high-resolution powder diffractometer (HRPD) at the ISIS neutron facility, Rutherford Appleton Laboratories.[21] For the low-temperature measurements, the powdered sample was lightly packed into an aluminum can of slab geometry, area 40 mm^2, 10 mm thick, with thin neutron-transparent vanadium windows front and back. The can was connected to the center stick, and the assembly was mounted in a Sumitomo 415 closed-cycle refrigerator with 60–80 mbar of He exchange gas. Heat was supplied to the sample through a 100-W cartridge heater inserted in the side wall of the sample can, and temperature was monitored through an Rh/Fe sensor located in the opposite wall. A gadolinium, neutron-absorbing mask was attached to the side of the can facing the incident beam and back-scattering detectors to prevent contaminant Bragg peaks arising from either the body of the sample can, including sensor and heater, or the stainless steel frames supporting the vanadium windows.

For the high-temperature measurements, the sample was housed in an 11 mm-diameter thin-walled, cylindrical vanadium can which was mounted in a standard ISIS furnace, and the whole furnace was evacuated to 5×10^{-4} mbar. All diffraction patterns were recorded over the time-of-flight range 30–130 ms in both the back-scattering and 90° detector banks, corresponding to d spacings from 0.6 to 2.6° A (at a resolution $\sim\Delta d/d$ 4×10^{-4}) and from 0.9 to 3.7° A ($\Delta d/d$ 2×10^{-3}), respectively, independent of d. The patterns were normalized and corrected for detector efficiency according to prior calibration with a vanadium scan. After recording a pattern at room temperature, the sample was cooled, then patterns recorded at 7 K, at 10 K, then in 10 K steps to 170 K, at 175 K, then in 5 K steps to 230 K, and finally in 10 K steps to 400 K. Data in the furnace were recorded at 290 K, 370 K, and then 10 K steps to 1000 K. In order to establish if any unusual phenomenon occurs in the sample after heating, a small number of patterns were collected as the sample was recooled, namely at 900, 800, and 700 K, and then at 50 K steps to 400 K. During all measurements, the temperature variation was less than ±2 K. The structures were refined using the Rietveld method as implemented in the GSAS[22] program. The background and peak widths were refined together with the lattice parameters, atomic positions, and isotropic and anisotropic atomic displacement parameters (ADP) for the cations and oxygen atoms, respectively. Anisotropic peak broadening, which became evident during refinements of the $I4/mcm$ tetragonal structure, was modeled using the peak-width description developed by Stephens.[23]

The cationic compositions were evaluated by a Carl Zeiss Evo 50 scanning electron microscope (SEM) with LaB_6 filament operated at 25 kV, equipped with an IXRF System energy dispersive spectroscopy (EDS) detector (EDS2006 version 1.0). The sample was analyzed as a sintered pellet that was mounted on an aluminum sample stub.

Magnetic susceptibility and magnetization measurements were carried out using a Quantum Design PPMS9 device in 0–9 T magnetic field and 2–390 K temperature range. The same device was used for the heat capacity measurements between 25 and 300 K using a thermal relaxation method.

III. RESULTS

A. Room temperature and variable temperature structural analysis

Scanning electron micrograph images established that the sample of $Sr_{0.65}Pr_{0.35}MnO_3$ was well sintered after heating at 1500 °C. Energy dispersive spectroscopy analysis at up to 10 different spots demonstrated the actual elemental composition to be that given by nominal composition. No evidence was found, either from the images or in EDS analysis, for any impurities or spurious features.

The neutron powder diffraction (NPD) pattern of $Sr_{0.65}Pr_{0.35}MnO_3$ recorded at room temperature was well fitted using a tetragonal structure in space group $I4/mcm$ with a = 5.382 30(5) and c = 7.780 87(8) Å. This tetragonal structure is a consequence of out-of-phase cooperative tilting about the c axis, of the corner-sharing MnO_6 octahedra, and is described using Glazer's notation as $a^0a^0c^-$.[24] This is the structure as indicated by a number of superlattice reflections, such as the 121 reflection (Fig. 1) associated with softening at the R point of the cubic Brillouin zone, in addition to well-resolved splitting of diagnostic Bragg reflections. The refinements provided no evidence for the presence of any anion vacancies.

Cooling the sample to below ~250 K resulted in the appearance of additional reflections in the NPD profiles, most noticeably at d = 2.0 and 2.4 Å, that were not indexed to $I4/mcm$ tetragonal cell, although the cell remained tetragonal. The intensity of these increased as the sample temperature

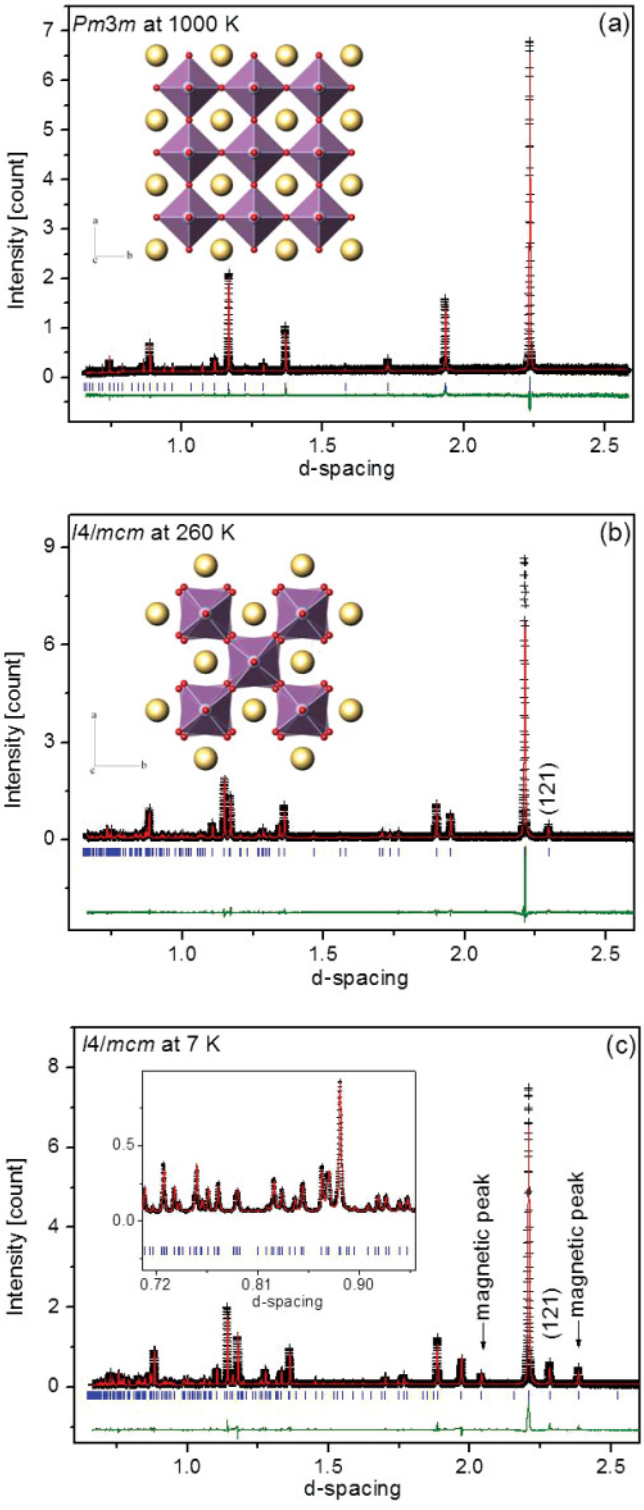

FIG. 1. (Color online) Observed, calculated, and difference neutron diffraction patterns for $Sr_{0.65}Pr_{0.35}MnO_3$ at 7, 260, and 1000 K. The crosses represent the data, the red/dark gray line is the calculated profile, the green/medium gray line is the difference profile, and vertical markers are the allowed Bragg reflections. The inserts (a) and (b) are representations of the refined cubic ($Pm\bar{3}m$) and tetragonal ($I4/mcm$) structures, respectively, where Sr,Pr; Mn; O. The inset (c) highlights the quality of both the neutron diffraction data and the fit.

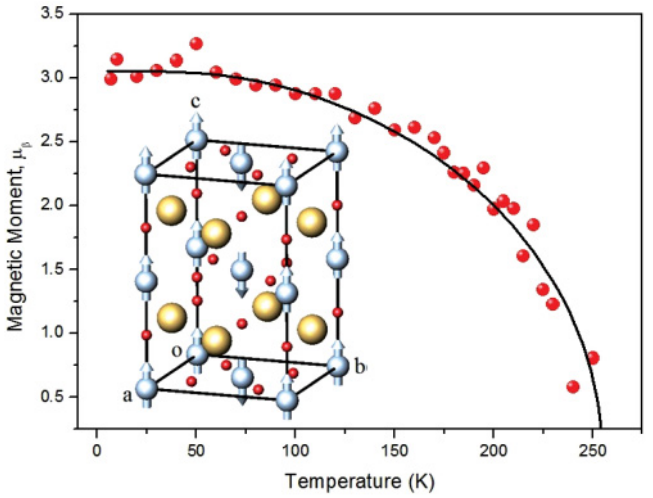

FIG. 2. (Color online) Temperature dependence of ordered magnetic moments in C-type AFM ground states of $Sr_{0.65}Pr_{0.35}MnO_3$. The solid line is a fit to a Brillouin function [Eq. (1)] with $T_N = 255$ K. The inset illustrates the Mn spin alignment in the C-type AFM ground state.

was lowered, reaching a constant value below ~150 K. These reflections are a consequence of magnetic ordering of the Mn cations. Analysis demonstrated that $Sr_{0.65}Pr_{0.35}MnO_3$ adopts a C-type antiferromagnetic structure with propagation vector (1/2, 1/2, 0) and spins aligned parallel to the c axis. This is the same magnetic structure observed previously in the closely related oxide $Sr_{0.9}Ce_{0.1}MnO_3$ (Ref. 25) and is consistent with the earlier work of Knizek *et al.*[7] Refinement of the nuclear and magnetic structures resulted in a good fit to the data. The temperature dependence of the refined magnetic moments is illustrated in Fig. 2 with the moment increasing from 0.805 μ_B/Mn at 250 K to ~3.0 μ_B/Mn at 7 K. The spin-only value for a mixture of 65% Mn^{4+} ($S = 3/2$) and 35% Mn^{3+} ($S = 2$) is ~4.2 μ_B/Mn. The reduction in the moment is a result of the strong hybridization of the Mn and O states in tetragonal $Sr_{0.65}Pr_{0.35}MnO_3$.[13]

The solid line in Fig. 2 shows the simulated $M(T)$ dependence, based on the mean field formula:[26]

$$M = M_0 B_S\left(\frac{3S}{S+1}\frac{T_N}{T}\frac{M}{M_0}\right), \quad (1)$$

where $M_0 = M(0\text{ K})$, S is the spin quantum number of the magnetic ion, T_N is the Neel temperature, and B_S is a Brillouin function. Good agreement with experimental data was obtained using $M_0 = 3.5\ \mu_B$, $T_N = 255$ K, and $S = 3/2$ (as most of magnetic moments are associated with Mn^{4+} ions).

Heating the sample above the Neel temperature of ~250 K resulted in a gradual reduction in the intensity of the R-point reflections, as well as in the splitting of diagnostic Bragg reflections, such that neither feature is apparent above 720 K. Above this temperature, the structure is cubic, and Rietveld analysis in space group $Pm\bar{3}m$ gave $a = 3.853\,42(1)$ Å. Establishing the precise transition temperature from the diffraction data is limited by the rapid decrease in the intensity and broadening of the R-point reflections, associated with the tilting of the

TABLE I. Details of the structures of $Sr_{0.65}Pr_{0.35}MnO_3$ at selected temperatures. In $Pm\bar{3}m$, Mn is located on Wyckoff 1*a* at (0,0,0), O on 3*d* at ($\frac{1}{2}$,0,0), while Sr and Pr share 1*b* at ($\frac{1}{2},\frac{1}{2},\frac{1}{2}$). In $I4/mcm$, Mn is on 4*c* at (0,0,0), Sr and Pr are disordered on the 4*b* positions ($0,\frac{1}{2},\frac{1}{4}$), and there are two crystallographically distinct O sites, O1 at 4*a* ($0,0,\frac{1}{4}$) and O2 at 8*h*, (x,$x+\frac{1}{2}$,0).

T (K)	7	170	260	350	500	1000
Space group	$I4/mcm$	$I4/mcm$	$I4/mcm$	$I4/mcm$	$I4/mcm$	$Pm\bar{3}m$
a (Å)	5.33078(5)	5.34636(7)	5.37363(6)	5.39495(7)	5.42016(2)	3.868679(9)
c (Å)	7.87983(8)	7.85083(11)	7.79694(10)	7.76025(12)	7.72670(5)	a
Vol (Å^3)	223.923(4)	224.405(5)	225.144(5)	225.866(5)	226.996(2)	57.9013(2)
R_p	0.0671	0.1019	0.0704	0.0792	0.1324	0.3472
R_{wp}	0.0849	0.1128	0.1070	0.1213	0.0612	0.0549
χ^2[a]	23.67	41.81	37.61	47.72	15.58	11.58
x (O2)	0.28337(7)	0.28174(10)	0.27833(10)	0.27465(14)	0.26889(12)	0.5
U(Å$^2 \times 10^2$)						
U_{iso} (Sr, Pr)	1.20(2)	1.29(2)	1.52(2)	1.66(3)	2.06(2)	3.17(2)
U_{iso} (Mn)	1.09(2)	1.24(4)	1.28(4)	1.35(5)	1.81(3)	2.16(3)
U_{11} (Mn)	1.59(2)	1.24(4)	1.28(4)	1.35(5)	1.81(3)	4.01(2)
U_{22} (Mn)	1.43(1)	1.62(3)	1.95(3)	2.18(4)	2.76(5)	
U_{iso} (O1)		1.62(3)	1.95(3)	2.18(4)	2.76(5)	
U_{11} (O1)		1.63(6)	1.78(5)	2.08(7)	3.05(7)	
U_{22} (O1)		1.37(2)	1.72(2)	1.80(3)	2.52(3)	
U_{33} (O1)		1.37(2)	1.72(2)	1.80(3)	2.52(3)	
U_{iso} (O2)		1.91(4)	2.11(4)	2.66(5)	4.05(5)	
U_{11} (O2)		0.19(3)	0.31(3)	0.44(4)	0.56(4)	
U_{22} (O2)						
U_{33} (O2)						
U_{13} (O2)						
Mn-O(1) (Å)	1.96996(2)	1.9627(3)	1.94923(2)	1.94091(3)	1.93168(1)	1.93438(2)
Mn-O(2) (Å)	1.90143(7)	1.90535(11)	1.91203(9)	1.91612(10)	1.92178(7)	
Mn-O(2)-Mn (°)	164.80(3)	165.53(5)	167.07(5)	168.62(6)	171.37(5)	180
μ_B/Mn	2.99(2)	2.87(4)				
Φ[b]	7.603(2)	7.24(2)	6.46(2)	5.63(4)	4.32(3)	
$\Delta d \times 10^3$[b]	41.1	34.4	22.3	14.8	5.94	

[a]The higher-than-typical χ^2 values in the tetragonal phase reflect the effects of domain wall broadening.
[b]Φ, octahedral tilt angle in degrees; Δd, octahedral distortion parameter.

octahedra, above ~650 K. Representative examples of the refined structures are presented in Table I.

The temperature dependence of the lattice parameters and cell volume for $Sr_{0.65}Pr_{0.35}MnO_3$, illustrated in Fig. 3, suggest the $I4/mcm$-to-$Pm\bar{3}m$ transition is continuous. The $Pm\bar{3}m \leftrightarrow I4/mcm$ phase transition appears to be reversible upon cooling. That $Sr_{0.65}Pr_{0.35}MnO_3$ undergoes an apparently continuous transition to a cubic structure near 720 K is in good agreement with the earlier x-ray studies by Knizek *et al.*[7] A small amount of hysteresis in the thermal expansion is observed upon recooling the sample. This is not unexpected, and it is possible that the structures are influenced by a small change in the oxidation state of the Mn. Recall that the high-temperature measurements are conducted in a high-vacuum furnace, and some reduction of the Mn is possibly not unexpected, although the structural refinements did not reveal the presence of any anion vacancies.

The lattice parameters of, and Mn-O bond lengths in, $Sr_{0.65}Pr_{0.35}MnO_3$ (Fig. 4) can be divided into three temperature regions, namely 7 ~ 250 K, 250 ~ 750 K, and above 750 K, suggesting two events occur. These correspond to the magnetic ordering transition with $T_N \sim 250$ K and a structural ($Pm\bar{3}m \leftrightarrow I4/mcm$) transition at ~750 K. The temperature dependence of the lattice parameters and bond distances between 7 and 250 K indicate that there is significant coupling between magnetism and the crystal lattice at low temperature. The anisotropy in the magnetostriction is consistent with a C-type AFM ground state.

The thermal behavior of the cell parameters above 250 K is very similar to that observed for $Sr_{0.8}Ce_{0.2}MnO_3$ and $Sr_{0.8}Ce_{0.2}Mn_{0.8}Co_{0.2}O_3$ by Zhang *et al.*,[27,28] and appears to be indicative of a continuous $Pm\bar{3}m$-$I4/mcm$ structural transition. In perovskites, the $Pm\bar{3}m$-$I4/mcm$ transition involves the softening of the R_4^+-zone boundary mode, and such an event is allowed to be continuous.[29]

Linear strains were calculated from the lattice parameters estimated in the Rietveld analysis of the neutron diffraction data, as described previously,[30] with $e_1 = e_2 = (a_e - a_o)/a_o$, $e_3 = (c_e - a_o)/a_o$. The reference parameter a_o for the cubic structure was obtained by fitting

$$V_o = V_1 + V_2\Theta\coth(\Theta/T) \quad (2)$$

to unit cell volume data in the interval 800–950 K and then taking $a_o = V_o^{1/3}$. The temperature Θ was included to account for the normal saturation of thermal expansion as $T \rightarrow 0$ K.

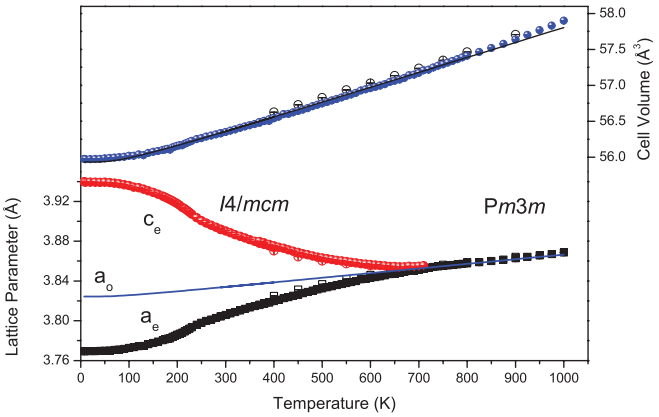

FIG. 3. (Color online) Temperature dependence of the reduced lattice parameters $a_e \approx a_p/\sqrt{2}$ and $c_e \approx a_p/2$ of $Sr_{0.65}Pr_{0.35}MnO_3$. The hollow symbols are from data collected during recooling the sample. Where not apparent, the estimated standard deviations are smaller than the symbols. The solid lines are fits from an equation of the form $V_o = V_1 + V_2\Theta\coth(\Theta/T)$, where $\Theta = 110$ K; see text for details.

This was fixed at 110 K, which is not unreasonable for thermal expansion of an oxide perovskite.[31] The linear strains were converted to symmetry-adapted strains e_a and e_t as:

$$e_a = e_1 + e_2 + e_3, \tag{3}$$

$$e_t = \frac{1}{\sqrt{3}}(2e_3 - e_1 - e_2). \tag{4}$$

The temperature dependences of e_a (volume strain) and e_t (tetragonal shear strain) obtained in this way are shown in Fig. 5. Although the absolute values of the volume strain are sensitive to the choice of baseline, the positive strain of up to ~0.005 is comparable with the volume strain up to ~0.008 due to Jahn–Teller (JT) distortions of $Mn^{3+}O_6$ in

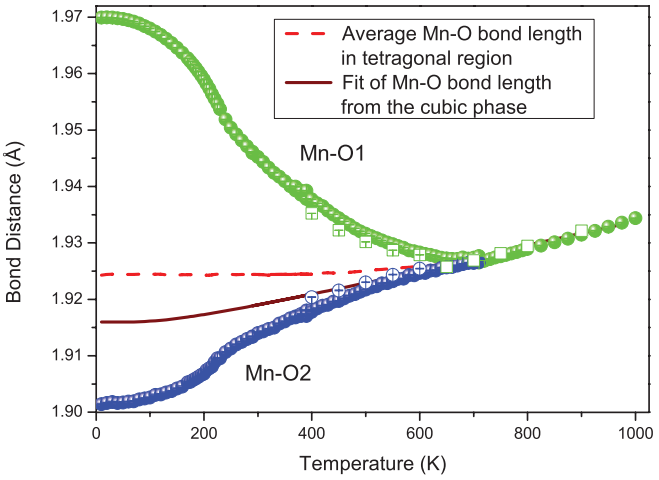

FIG. 4. (Color online) Temperature dependence of the Mn-O bond lengths in $Sr_{0.65}Pr_{0.35}MnO_3$. The hollow symbols are from data obtained during recooling of the sample. Where not apparent, the esds are smaller than the symbols. The solid line is a fit of the bond distances in the cubic phase to an equation similar to Eq. (2), and the dashed line is the average Mn-O distance.

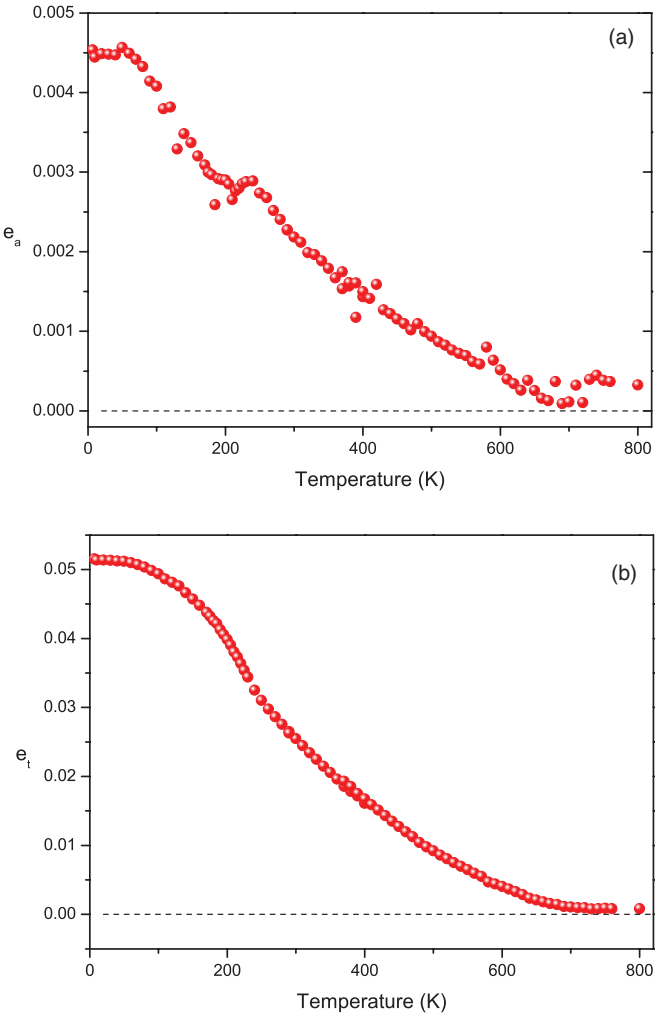

FIG. 5. (Color online) The temperature dependence of (a) the volume strain e_a and (b) the tetragonal shear strain e_t.

$LaMnO_3$.[32] That $LaMnO_3$ has a larger value probably reflects the presence of more Mn^{3+} cations in this compound compared to $Sr_{0.65}Pr_{0.35}MnO_3$. The values of e_t are relatively insensitive to the choice of a_o and display an unusual pattern of evolution, which suggests that they include contributions from more than one structural influence. Indeed neither e_t nor e_t^2 vary linearly with temperature, but rather, as illustrated in Fig. 6, a plot of $e_t^{0.5}$ against temperature is linear. This matter will be discussed further in Subsec. C below.

B. Tilting and distortion of the MnO_6 octahedra

The magnitudes of the out-of-phase tilts were obtained from the refined atomic coordinates. The temperature dependence of the square of the octahedral tilt angle, Φ^2, is shown in Fig. 7. A standard Landau solution to describe a second-order tilting transition would be:[33]

$$\Phi^2 = A\frac{\Theta_s}{T_c}\left[\coth\left(\frac{\Theta_s}{T_c}\right) - \coth\left(\frac{\Theta_s}{T}\right)\right], \tag{5}$$

where Θ_s is the order parameter saturation temperature, and A is a constant. At temperatures well above 0 K, this gives a linear relationship in the normal way, and a linear fit to

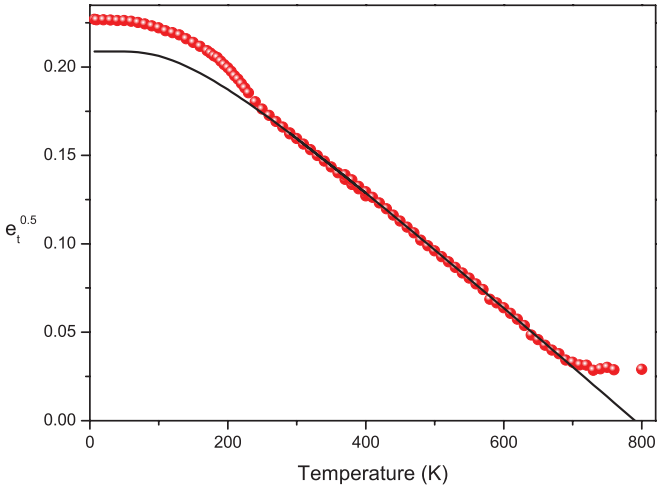

FIG. 6. (Color online) Temperature dependence of $e_t^{0.5}$ illustrating linear dependence in the paramagnetic region. The line is a fit to an equation similar to Eq. (2) using data points between 250 and 700 K; Θ was fixed at 110 K.

the data between 430 and 680 K gives $T_c = 732$ K (straight line in Fig. 7). Saturation effects should lead to a leveling off of Φ^2 as $T \rightarrow 0$ K, but instead, a marked increase in slope below ~300 K is observed before the plateau region is reached. This implies a coupling between the magnetic ordering and octahedral tilting.

The Mn-O bond distances in $Sr_{0.65}Pr_{0.35}MnO_3$ evolve continuously between 250 and 750 K, albeit not with a constant rate. The cubic perovskite has six equal Mn-O bonds. In the tetragonal structure, the MnO_6 octahedra are tilted relative to each other as a result of the conflicting bonding requirements of the *A*- and *B*-type cations. These tilts can introduce distortions of the BO_6 octahedra, although such distortions are typically small.[34] Through a comparison with the results for $SrZrO_3$, it is evident that the magnitude of

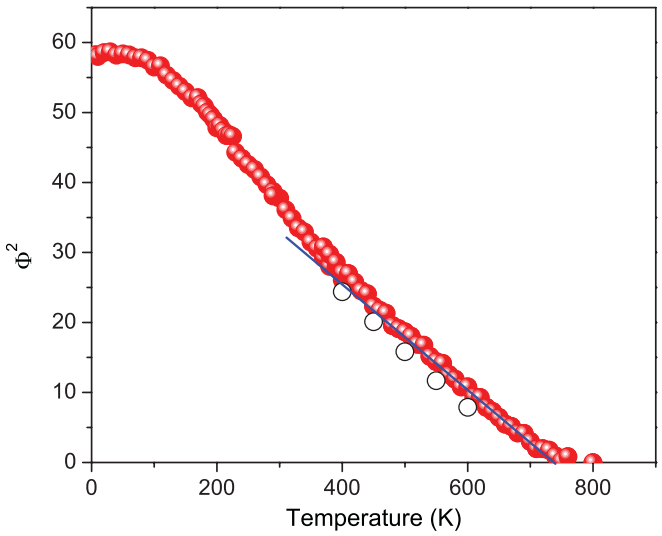

FIG. 7. (Color online) Temperature dependence of the square of tilt angle, Φ^2 in $Sr_{0.65}Pr_{0.35}MnO_3$. The hollow symbols are from data obtained during recooling of the sample. The solid line is a linear fit to data between 430 and 680 K, which extrapolates to zero at 732 K.

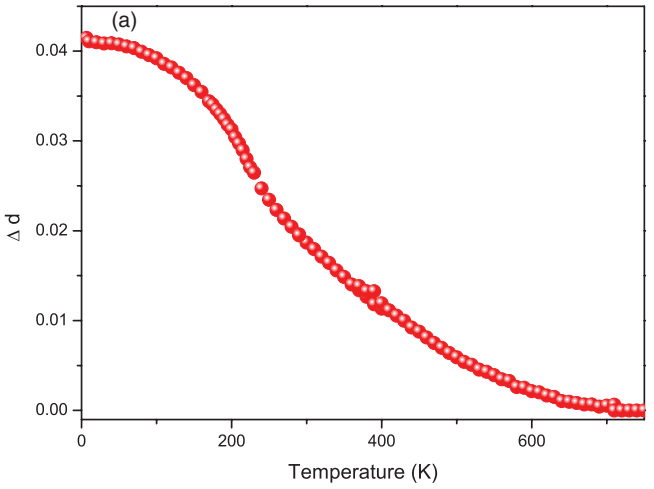

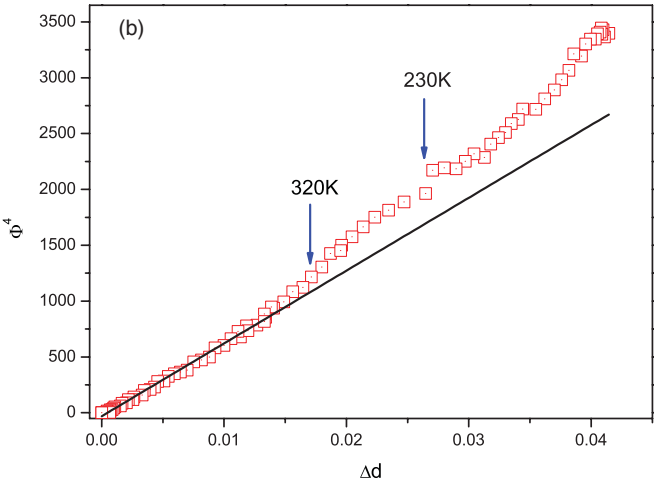

FIG. 8. (Color online) (a) Temperature dependence of the distortion parameter $\Delta d = \frac{1}{\sqrt{3}}\left(\frac{2d_{Mn-O1}-2d_{Mn-O2}}{(1/3)(d_{Mn-O1}+2d_{Mn-O2})}\right)$ in $Sr_{0.65}Pr_{0.35}MnO_3$. (b) The tetragonal distortion varies linearly with Φ^4 at high temperatures, but there are anomalies associated with changes in magnetic properties evident at lower temperatures. The solid line in (b) is a linear fit to the high temperature data.

the distortion of the MnO_6 octahedra below, say, 500 K is larger than expected from tilting alone. For example, at 350 K (around 400 K below the transition to cubic), the two Mn-O1 bonds are noticeably (0.024 79 Å or 1.3%) longer than the four Mn-O2 bonds (Table I) 1.940 91(3) vs 1.916 12(10) Å. $SrZrO_3$ is orthorhombic 400 K below T_c with a small compression of the ZrO_6 octahedra of ~0.55%.[18] The tetragonal strains, too, are larger than in other perovskites (see Subsec. C and references[30,35,36]). The larger strains and distortions here are attributed to a JT-type distortion.

The extent of the tetragonal distortion of the MnO_6 octahedra can be quantified by a distortion parameter Δd,

$$\Delta d = \frac{1}{\sqrt{3}}\left(\frac{2d_{Mn-O1} - 2d_{Mn-O2}}{(1/3)(d_{Mn-O1} + 2d_{Mn-O2})}\right), \qquad (6)$$

defined by analogy with the tetragonal strain [Eq. (4)]. As illustrated in Fig. 8(a), this increases nonlinearly below ~720 K, has a marked break in slope near 250 K, and reaches a plateau below ~75 K. Similarity to the temperature variation

shown in Fig. 5(b) suggests that the overall tetragonal strain is dominated by the distortion of the MnO_6 octahedra. The initial increase is a consequence of the octahedral tilting combined with the JT distortion. An interdependence of the octahedral distortion and tilting is clearly evident from Fig. 8(b), where surprisingly, Δd varies with Φ^4, rather than Φ^2, as expected for a second-order JT transition, in the high-temperature range. In addition, there is evidence for the influence of magnetism on the structure with changes in slope at ~320 and 250 K. Bulk susceptibility measurements, presented in Subsec. D, provide evidence for the formation of superparamagnetic clusters around 320 K, while the neutron diffraction measurements showed (Fig. 2) that long-range antiferromagnetic ordering occurs around 250 K.

C. The influence of coupling of the octahedral tilting, Jahn–Teller distortions, and magnetostriction on the strains

At least three structural contributions are likely to be present in the strain variations, i.e. octahedral tilting, Jahn–Teller distortions, and magnetostriction, though the latter will be ignored in the first instance. An overview of combined JT and tilting transitions has been given by Carpenter and Howard[32,37] and forms the basis for the present analysis. The combined effect of these in $Sr_{0.65}Pr_{0.35}MnO_3$ gives space group $I4/mcm$, for which the relevant JT order parameter belongs to irreducible representation (irrep) Γ_3^+, and the relevant tilting parameter belongs to irrep R_4^+ of space group $Pm\bar{3}m$ (Table I of Carpenter and Howard[37]). These have components (a,0) and (b,0,0), respectively, and the nonzero components are labeled Q_{JT} and Q_{tilt} here. For practical purposes, these can be identified with the Δd and Φ of Sec. III B. The observed symmetry adapted strains, e_t and e_a, contain contributions from the coupling with these two order parameters. The JT contribution can be described by the distortion of the octahedra and should vary as $e_a \propto {e_t}^2 \propto {Q_{JT}}^2$, while the tilting contribution is expected to vary as $e_a \propto e_t \propto {Q_{tilt}}^2$. Coupling between the order parameters themselves can occur indirectly via common strains or directly, with the form $\lambda {Q_{tilt}}^2 Q_{JT}$.[38]

If there are two separate instabilities with quite similar T_c values and the coupling between these is strong, we might expect to see ${Q_{tilt}}^2 \propto Q_{JT}$ and a single transition point T_c. The Landau free energy expansion for Q_{JT} is allowed to contain odd order terms,[38] and the JT transition by itself would be expected to be first order in character. One limiting case would be a single transition which is tricritical in Q_{tilt} and second order in Q_{JT}. This would give ${Q_{tilt}}^4 \propto {Q_{JT}}^2 \propto (T_c - T)$, with strains that follow accordingly. If the tilting transition is second order and the coupling is strong, we would expect to see ${Q_{tilt}}^2 \propto Q_{JT} \propto (T_c - T)$, with the outcome of $Q_{JT} \propto (T_c - T)$. If the two transition temperatures were very different, we would expect to see a single T_c but some crossover behavior at lower temperatures near the second instability (see for example Refs. 37 and 39). $Sr_{0.65}Pr_{0.35}MnO_3$ does not meet any of these expectations. Rather, as shown by considering the strain/strain/tilt angle relationships, it shows a unique strain evolution.

Figure 9 shows the tetragonal (e_t) and volume (e_a) strains plotted against Φ^2, while Fig. 6 shows ${e_t}^{0.5}$ plotted against temperature. That e_a scales approximately linearly with Φ^2

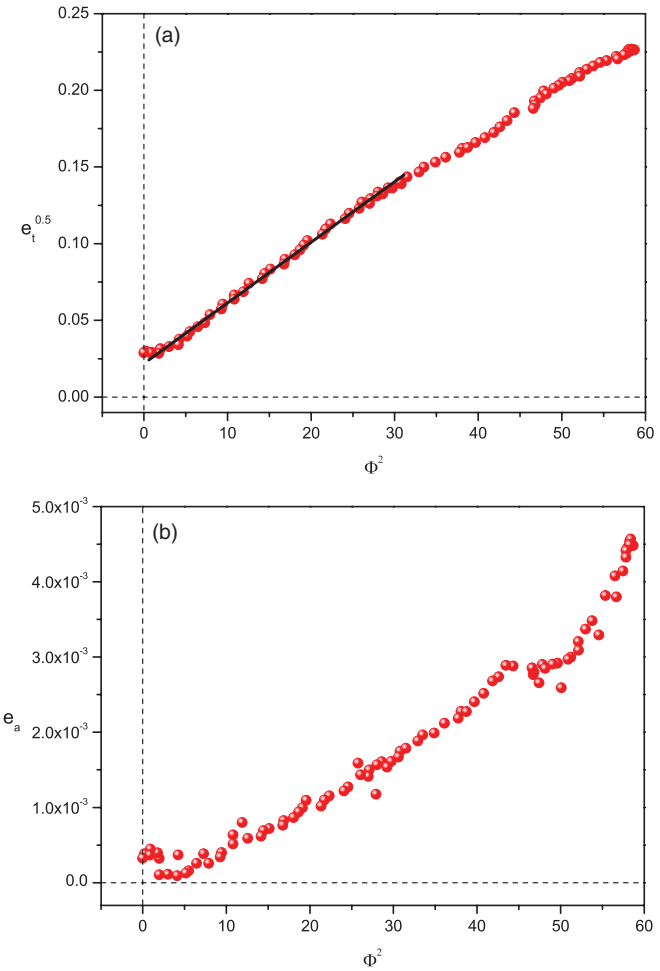

FIG. 9. (Color online) (a) The square root of the tetragonal strain e_t shows a linear dependence on the square of the tilt angle at high temperatures. At low temperatures, this relationship breaks down due to the influence of magnetic interactions. The straight line is a fit to the data between 450 and 670 K. (b) The volume strain e_a shows a linear dependence on the square of the tilt angle, except at low temperatures, where magnetic effects become important.

is as expected for a normal second-order tilting transition, though with irregularities at lower temperatures [$\Phi^2 > \sim 45$ in Fig. 9(b)] that may relate to the magnetic ordering described below. The unusual result is ${e_t}^{0.5} \propto {Q_{tilt}}^2$ [Fig. 9(a)], i.e. $e_t \propto {Q_{tilt}}^4$ instead of $e_t \propto {Q_{tilt}}^2$. A similarly unusual behavior ($e_t \propto {Q_{tilt}}^4$) has been noted in $Sr_{0.8}Ce_{0.2}MnO_3$ (Ref. 28). Apart from the nonzero value of e_t at ~730 K where $\Phi \to 0$, the transition could be characterized as having ${e_t}^{0.5} \propto (T_c - T)$ with close adherence to Eq. (1) [$\Theta_s = 175$ K for the fit to data between 250 and 700 K in Fig. 9]. Below 250 K, the influence of magnetic ordering is again clearly visible. The magnitude of the shear strain reaches ~5% at 0 K, which is much greater than would be expected for a normal tilting transition (<1% in $LaAlO_3$, for example[40]). This is further evidence for the JT distortions playing a major role in the overall strain behavior. If the discontinuity in e_t at ~730 K is real and not due to some artifact of refinements when the distortion from cubic lattice geometry is very small, there are two possible explanations. The transition could be just first order, or it may be driven by

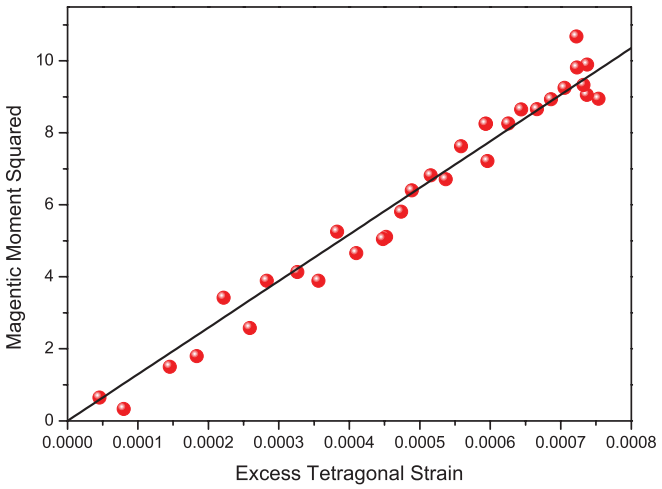

FIG. 10. (Color online) Relationship between the excess tetragonal strains estimated from the data shown in Fig. 6 and the square of the magnetic moment per Mn obtained from the neutron diffraction data. The solid line is a linear fit constrained to pass through the origin.

tilting of octahedra which are already locally distorted from cubic geometry in the high-temperature phase. A very small discontinuity in Δd is observed at the same temperature.

To summarize, there is, for temperatures above the magnetic ordering transition point, a second-order tilting transition with $T_c \sim 730$ K in which there is strong coupling with tetragonal distortions of the MnO_6 octahedra. There is no overt evidence of two separate structural instabilities. If it is assumed that the tetragonal shear strain can be attributed essentially to the influence of Q_{JT} alone (i.e. for relatively weak coupling of e_t with Q_{tilt}), it follows that the effective coupling between Q_{tilt} and Q_{JT} has the form $\lambda {Q_{tilt}}^4 Q_{JT}$ to give $Q_{JT} \propto {Q_{tilt}}^4$. Favorable coupling between these two order parameters would occur if the volume strains coupled to each have the same sign. In effect, an increase in the JT distortion, which correlates with an increase in volume strain, causes an increase in the tilt angle. Here, $\lambda {Q_{tilt}}^4 Q_{JT}$ is allowed by symmetry, but we do not have an explanation for why this term should be large in comparison with $\lambda {Q_{tilt}}^2 Q_{JT}$, which would more normally be expected to be dominant. A rather similar result, namely octahedral distortion $\propto \Phi^4$, has previously been noticed in rhombohedral $LaCoO_3$.[41]

From Fig. 6, it is clear that the magnetic transition gives rise to some additional tetragonal strain. The excess strain below 250 K can be quantified from the difference between the observed values of strain and the fitted values corresponding to the solid line in Fig. 6. Taking the magnetic moment, estimated from the neutron diffraction data, as the order parameter $Q_{magnetic}$, we observe in Fig. 10 that the excess strain e_t is proportional to ${Q_{magnetic}}^2$, as anticipated.[42] This raises the interesting question of how the additional strain introduced by the magnetic ordering is manifested in the observed structure. Examination of Fig. 8 reveals that the magnetic ordering results in an increase in the tilt angle, showing there to be effective coupling between the magnetic ordering process and octahedral tilting. Magnetic ordering alone is not expected to alter the tilting of the MnO_6 octahedra; however, it appears that the magnetic ordering induces a change in the JT distortion, which in turn results in a change in the tilt angle. That the tilt angles below T_N (see Figs. 6 and 7) are larger than expected reflects an increase in the effective size of the Mn cation due to the enhancement of the JT distortion by magnetic ordering.

D. Physical characterization

The temperature dependence of the *dc* magnetic susceptibility χ is shown in Fig. 11. Exchange interactions between the Mn and Pr subsystems are weak, and the total susceptibility is a sum of the Curie–Weiss term for Mn and the Curie-type term for Pr. At high temperatures, above 320 K, the magnetic susceptibility follows the Curie–Weiss law $\chi(T) = \frac{C}{T-\Theta_{CW}}$, where C is the Curie constant and Θ_{CW} the characteristic Curie–Weiss temperature. The value of C obtained from a least square fit is $C = 4.9$ emu K mole^{-1}, which is equivalent to an anomalously high effective moment of $\mu_{eff} = 6.13\,\mu_B$/f.u. The estimated value of Θ_{CW} is 97.3 K. The theoretical spin-only value ${\mu_{eff}}^{th}$, calculated assuming the oxidation states ratios $Pr^{3+}:Mn^{3+}:Mn^{4+}$ are 0.35:0.35:0.65, equal to 4.76 μ_B/f.u., is somewhat smaller than the observed value. We believe this reflects the formation of superparamagnetic clusters, as commonly observed among manganites,[43] although the possibility that the actual Pr^{3+} Mn^{3+} Mn^{4+} ratio is different to the expected value cannot be totally excluded. The formation of a superparamagnetic state assumes grouping of neighboring magnetic spins with these acting as a cluster with a large magnetic moment via Mn^{3+}-O-Mn^{4+} double-exchange paths. This leads to an increase in both the Curie–Weiss constant and the effective magnetic moment. The large positive characteristic Θ_{CW} temperature suggests ferromagnetic interactions dominate in $Sr_{0.65}Pr_{0.35}MnO_3$ above 320 K, which is consistent with the formation of superparamagnetic clusters. At 320 K, the susceptibility shows a deviation from Curie–Weiss behavior, there being an increase in the magnetic susceptibility,

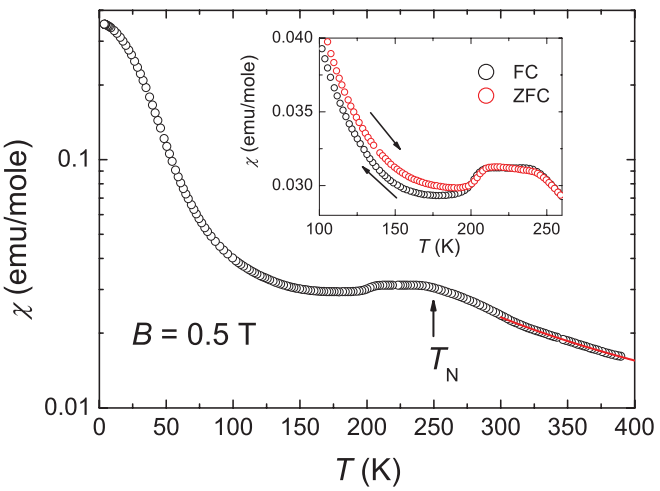

FIG. 11. (Color online) Temperature dependence of magnetic susceptibility $\chi(T)$ of $Sr_{0.65}Pr_{0.35}MnO_3$ recorded with an applied magnetic field of 0.5 T. The solid line is the Curie–Weiss law fit (for details, see the text). The inset shows the field cooled (FC)–zero-field cooled (ZFC) curves at the vicinity of the $T_N = 150$ K.

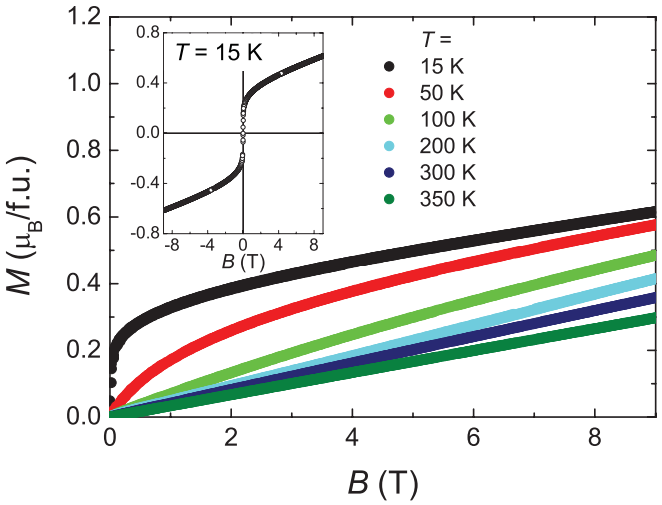

FIG. 12. (Color online) Field dependencies of magnetization M collected at various temperatures. The inset shows the full hysteresis curve obtained at 15 K.

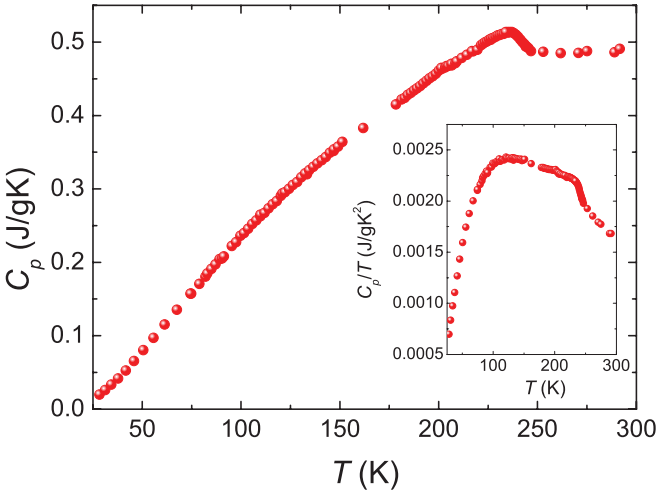

FIG. 13. (Color online) Temperature dependence of heat capacity $C_p(T)$ of $Sr_{0.65}Pr_{0.35}MnO_3$. Inset shows the C_p/T ratio.

suggestive of the onset of a weak ferromagnetic contribution to the susceptibility. Cooling to 240 K produces a plateau in $\chi(T)$, which drops again as the temperature is decreased below 210 K. This flat, extended anomaly is believed to be associated with the onset of long-range antiferromagnetic ordering at $T_N = 250$ K, seen in the NPD data. Below 170 K, there is a rapid increase in $\chi(T)$, which tends to saturate at the lowest temperatures, where the effects of the crystal field splitting of the Pr^{3+} ions may become important. Although the feature near T_N is broad, there is no evidence in the diffraction data to suggest the presence of the A-type $Fmmm$ phase, as seen in $Sr_{0.60}Pr_{0.40}MnO_3$ with $T_N \sim 200$ K.[7]

Figure 12 shows the field dependencies of magnetization M collected in various temperatures. A $T = 15$ K, the hysteresis curve (the inset in Fig. 12) reveals very low-remnant magnetization (~0.05 μ_B/f.u.) and coercive field (~0.003 T) in the presence of a relatively high-saturation moment, up to 0.6 μ_B/f.u. at 9 T and 15 K. The origin of the ferromagnetic-like behavior at low temperatures in many manganites is still unclear; however, it is usually explained in terms of canted order[44] or spin/cluster-glass state,[45] coexisting with the majority antiferromagnetically ordered phase. The latter appears to be appropriate in the present case, based on: the collinear magnetic structure suggested by NPD and the extremely narrow hysteresis loop and slight branching of the field cooling (FC)–zero-field cooling (ZFC) curves shown in the inset of Fig. 11; it is typical for spin glasses to be associated with some irreversibility and presence of superparamagnetic state at high temperatures.[46] A Brillouin-like magnetic response of the rare earth ions may also contribute to the observed magnetization, and this may be responsible both for saturation of magnetic susceptibility $\chi(T)$ and curvature of $M(B)$ at the lowest temperatures. The $M(B)$ curves collected at higher temperatures are typical of those observed in antiferromagnets (above 150 K) and paramagnets (above 300 K), i.e. $M(B) \sim B$.[47]

It is worth noting that conductivity measurements between 5 and 300 K demonstrated that that sample is semiconducting and that there is a substantial increase of the resistivity below T_N. This increase is believed to be related to charge carrier localization that accompanies the onset of long-range AFM ordering.

The temperature dependence of the heat capacity C_p of $Sr_{0.65}Pr_{0.35}MnO_3$ was also investigated, and these results are depicted in Fig. 13. The most striking feature of this figure is the anomaly with a maximum at $T = 236$ K. This is a consequence of the antiferromagnetic transition seen in both the neutron diffraction and bulk susceptibility measurements. The total heat capacity contains contributions from the lattice, electronic, and magnetic effects. As a consequence of the lack of a suitable isostructural compound (an isostructural oxide without localized d and f electrons), we were not able to estimate magnetic entropy released during the phase transition. The broad and extended anomaly in the heat capacity (and magnetic susceptibility) below the ordering temperature demonstrates the presence of structural/magnetic/charge disorder in $Sr_{0.65}Pr_{0.35}MnO_3$, typical for manganites.[48]

IV. SUMMARY AND CONCLUSION

$Sr_{0.65}Pr_{0.35}MnO_3$ below 750 K adopts a tetragonal $I4/mcm$ structure. Temperature-dependent powder neutron diffraction data show that it undergoes a low-temperature magnetic transition to a C-type antiferromagnet with $T_N \sim 250$ K, in good agreement with bulk susceptibility and heat capacity measurements. We demonstrate that the high-temperature $Pm\bar{3}m \leftrightarrow I4/mcm$ phase transition of $Sr_{0.65}Pr_{0.35}MnO_3$ can be interpreted using a single Landau free-energy expansion, which includes the contributions of both octahedral tilting and Jahn–Teller distortions. At temperatures above T_N, both the volume strain e_a and square of the octahedral tilt angle Φ^2 are proportional to $T_c - T$, as expected for a second-order phase transition. For a pure-tilting transition, it is expected that the tetragonal strain e_t would be proportional to the volume strain; however, this is not observed; rather $e_t^{0.5} \propto (T_c - T)$, probably as a consequence of the Jahn–Teller-type distortion, which is manifested by a larger-than-typical distortion of the MnO_6 octahedra.

At temperatures below 250 K, the effect of magnetostriction is evident in the tetragonal strain and in the distortion of the MnO_6 octahedra. The magnetic order increases the magnitude of the tetragonal strain e_t above what would otherwise be expected. The formation of superparamagnetic clusters near 320 K results in a small, but discernable, change in the distortion of the MnO_6 octahedra. Changes in the tilt angle upon magnetic ordering show there to be effective coupling between the magnetic ordering process and octahedral tilting.

ACKNOWLEDGMENTS

This work was supported by the Australian Research Council. The measurements at ISIS were supported by a beamtime allocation from the Science and Technology Facilities Council and by the Australian Research Council LIEF Grant "Access for Australian Researchers to Advanced Neutron Beam Techniques", AINSE, and the Access to Major Research Facilities Programme.

*b.kennedy@chem.usyd.edu.au

[1] J. B. Goodenough, Phys. Rev. **100**, 564 (1955).

[2] R. von Helmolt, J. Wecker, B. Holzapfel, L. Schultz, and K. Samwer, Phys. Rev. Lett. **71**, 2331 (1993).

[3] J. W. Lynn, C. P. Adams, Y. M. Mukovskii, A. A. Arsenov, and D. A. Shulyatev, J. Appl. Phys. **89**, 6846 (2001).

[4] X. Q. Huang, L. Pei, Z. G. Liu, Z. Lu, Y. Sui, Z. N. Qian, and W. H. Su, J. Alloy. Compd. **345**, 265 (2002).

[5] S. T. Aruna, M. Muthuraman, and K. C. Patil, Solid State Ion. **120**, 275 (1999).

[6] P. Decorse, G. Caboche, and L. C. Dufour, Solid State Ion. **117**, 161 (1999).

[7] K. Knizek, J. Hejtmanek, Z. Jirak, C. Martin, M. Hervieu, B. Raveau, G. Andre, and F. Bouree, Chem. Mat. **16**, 1104 (2004).

[8] K. Kikuchi, H. Chiba, M. Kikuchi, and Y. Syono, J. Solid State Chem. **146**, 1 (1999).

[9] C. N. R. Rao, P. N. Santhosh, R. S. Singh, and A. Arulraj, J. Solid State Chem. **135**, 169 (1998).

[10] R. D. Shannon, Acta Crystallogr. Sect. A **32**, 751 (1976).

[11] W. Boujelben, M. Ellouze, A. Cheikh-Rouhou, J. Pierre, Q. Cai, W. B. Yelon, K. Shimizu, and C. Dubourdieu, Phys. Status Solidi A **191**, 243 (2002).

[12] R. Sondena, P. Ravindran, S. Stolen, T. Grande, and M. Hanfland, Phys. Rev. B **74**, 144102 (2006).

[13] M. Chakraborty, P. Pal, and B. R. Sekhar, Solid State Commun. **145**, 197 (2008).

[14] Z. Jirak, S. Krupicka, Z. Simsa, M. Dlouha, and S. Vratislav, J. Magn. Magn. Mater. **53**, 153 (1985).

[15] D. Sanchez, J. A. Alonso, and M. J. Martinez-Lope, J. Chem. Soc. Dalton Trans. 4422 (2002).

[16] T. K. Y. Wong, B. J. Kennedy, C. J. Howard, B. A. Hunter, and T. Vogt, J. Solid State Chem. **156**, 255 (2001).

[17] L. Q. Li, B. J. Kennedy, Y. Kubota, K. Kato, and R. F. Garrett, J. Mater. Chem. **14**, 263 (2004).

[18] C. J. Howard, K. S. Knight, B. J. Kennedy, and E. H. Kisi, J. Phys. Condens. Matter **12**, L677 (2000).

[19] B. J. Kennedy, B. A. Hunter, and J. R. Hester, Phys. Rev. B **65**, 224103 (2002).

[20] G. J. Thorogood, M. Avdeev, M. L. Carter, B. J. Kennedy, J. Ting, and K. S. Wallwork, Dalton Transactions **40**, 7228 (2011).

[21] R. M. Ibberson, W. I. F. David, and K. S. Knight, The High-Resolution Powder Diffractometer (HRPD) at ISIS—a User Guide, Report, RAL-92-031 (Rutherford Appleton Laboratory, Chilton, Didcot, England, 1992).

[22] A. C. Larson and R. B. von Dreele, General Structure Analysis System (GSAS) Los Alamos National Laboratory Report No LAUR 86-748, 2004.

[23] P. W. Stephens, J. Appl. Crystallogr. **32**, 281 (1999).

[24] A. M. Glazer, Acta Crystallogr. Sect. B **28**, 3384 (1972).

[25] A. Sundaresan, J. L. Tholence, A. Maignan, C. Martin, M. Hervieu, B. Raveau, and E. Suard, Eur. Phys. J. B **14**, 431 (2000).

[26] B. I. Bleaney and B. Bleaney, *Electricity and Magnetism*, 3rd ed. (Oxford University Press, Oxford, 1989).

[27] Z. M. Zhang, B. J. Kennedy, C. J. Howard, L. Y. Jang, K. S. Knight, M. Matsuda, and M. Miyake, J. Phys. Condens. Matter **22**, 445401 (2010).

[28] Z. M. Zhang, C. J. Howard, B. J. Kennedy, M. Matsuda, and M. Miyake, J. Phys. Condens. Matter **21**, 124218 (2009).

[29] G. Shirane and Y. Yamada, Phys. Rev. **177**, 858 (1969).

[30] M. A. Carpenter, A. I. Becerro, and F. Seifert, Am. Miner. **86**, 348 (2001).

[31] R. E. A. McKnight, B. J. Kennedy, Q. Zhou, and M. A. Carpenter, J. Phys. Condens. Matter **21**, 015902 (2009).

[32] M. A. Carpenter and C. J. Howard, Acta Crystallogr. Sect. B **65**, 147 (2009).

[33] M. A. Carpenter, H. W. Meyer, P. Sondergeld, S. Marion, and K. S. Knight, Am. Miner. **88**, 534 (2003).

[34] B. J. Kennedy, C. J. Howard, and B. C. Chakoumakos, J. Phys. Condens. Matter **11**, 1479 (1999).

[35] R. E. A. McKnight, C. J. Howard, and M. A. Carpenter, J. Phys. Condens. Matter **21**, 14 (2009).

[36] M. A. Carpenter, Am. Miner. **92**, 309 (2007).

[37] M. A. Carpenter and C. J. Howard, Acta Crystallogr. Sect. B **65**, 134 (2009).

[38] M. A. Carpenter, C. J. Howard, B. J. Kennedy, and K. S. Knight, Phys. Rev. B **72**, 024118 (2005).

[39] E. Salje and V. Devarajan, Phase Transitions **6**, 235 (1986).

[40] S. A. Hayward, F. D. Morrison, S. A. T. Redfern, E. K. H. Salje, J. F. Scott, K. S. Knight, S. Tarantino, A. M. Glazer, V. Shuvaeva, P. Daniel, M. Zhang, and M. A. Carpenter, Phys. Rev. B **72**, 054110 (2005).

[41] Z. Y. Zhang, J. Koppensteiner, W. Schranz, D. Prabhakaran, and M. A. Carpenter, J. Phys. Condens. Matter **23**, 145401 (2011).

[42] J. C. Toledano and P. Toledano, *Landau Theory of Phase Transition*. (World Scientific, Singapore, 1987).

[43] J. C. Nie, J. H. Wang, and B. R. Zhao, J. Magn. Magn. Mater. **192**, L379 (1999).

[44] K. Hagdorn, D. Hohlwein, J. Ihringer, K. Knorr, W. Prandl, H. Ritter, H. Schmid, and T. Zeiske, Eur. Phys. J. B **11**, 243 (1999).

[45] A. Maignan, C. Martin, G. Van Tendeloo, M. Hervieu, and B. Raveau, J. Mater. Chem. **8**, 2411 (1998).

[46] X. L. Wang, J. Horvat, H. K. Liu, and S. X. Dou, Solid State Commun. **108**, 661 (1998).

[47] C. Kittel, *Introduction to Solid State Physics*, 8th ed. (Wiley, New Caledonia, 2005).

[48] N. Hu, C. L. Lu, K. F. Wang, L. Cheng, Y. Liu, J. M. Liu, R. Xiong, and J. Shi, Appl. Phys. A **103**, 485 (2011).